ARTICLE

Nanostructured Ruthenium Oxide Electrodes via High-Temperature Molecular Templating for Use in Electrochemical Capacitors

Michael T. Brumbach,* Todd M. Alam, Paul G. Kotula, Bonnie B. McKenzie, and Bruce C. Bunker

Sandia National Laboratories, Albuquerque, New Mexico 87185

ABSTRACT Ruthenium oxide is a model pseudocapacitive materials exhibiting good electronic and protonic conduction and has been shown to achieve very high gravimetric capacitances. However, the capacitance of thermally prepared ruthenium oxide is generally low because of low protonic conductivity resulting from dehydration of the oxide upon annealing. High-temperature processing, however also produces the electrically conducting ruthenium oxide rutile phase, which is of great interest for electrochemical capacitors. Here, unusual electrochemical characteristics were obtained for thermally prepared ruthenium oxide when fabricated in the presence of alkyl-thiols at high temperature. The performance characteristics have been attributed to enhanced multifunctional properties of the material resulting from the novel processing. The processing method relies on a simple, solution-based strategy that utilizes a sacrificial organic template to sterically direct hierarchical architecture formation in electro-active ruthenium oxide. Thin films of the templated RuO_2 exhibit energy storage characteristics comparable to hydrous ruthenium oxide materials formed under dramatically different conditions. Extensive materials characterization has revealed that these property enhancements are associated with the retention of molecular-sized metal oxide clusters, high hydroxyl concentrations, and formation of hierarchical porosity in the ruthenium oxide thin films.

KEYWORDS: electrodes • ruthenium oxide • templating • nanostructures • thin films • electrical energy storage • ultracapacitor

INTRODUCTION

Electrochemical capacitors (i.e., supercapacitors, double layer capacitors, or ultracapacitors) are defined by their ability to achieve a combination of power and energy density not available to either dielectric capacitors or batteries. Batteries can achieve high energy densities, whereas capacitors, with very low energy densities, are able to deliver high power (1, 2). High energy densities in batteries are a result of efficient utilization of the electrode material for charge storage; however, charge storage mechanisms are limited by several processes including slow reaction kinetics and electron and ion transport in the bulk, resulting in lower overall power delivery. Ultracapacitors can potentially achieve high energy and power densities simultaneously by incorporating electroactive materials, similar to those found in batteries, into high surface area configurations. Consequently, all sites in the active electrode (both surface and bulk) can be used for charge storage (boosting energy densities), whereas electroactive sites would be sufficiently close to electrolyte interfaces to allow for facile electron and ion transport (boosting power densities).

Electrochemical capacitors can store charge via two mechanisms, physical and chemical, where one is typically predominant (3, 4). High surface area carbon supercapacitors store charge in the electrical double layer at the charged interface of the carbon electrode and the electrolyte solution. Alternatively, redox active electrochemical capacitors, i.e., pseudocapacitors, are exemplified by the charge storage properties of ruthenium oxide where ruthenium oxidation/reduction is accompanied by proton adsorption/desorption.

$$RuO_2 + xH^+ + xe^- \leftrightarrow RuO_{2-x}(OH)_x \qquad (1)$$

We consider RuO_2 a model oxide for interrogation of our templated synthesis strategy because of the wealth of information available for this oxide system. Hydrous ruthenium oxide has been extensively studied as a material for ultracapacitors and exhibits exceptional performance. The oxide has access to multiple redox states and is a good electronic and/or protonic conductor. Notably, RuO_2 also has practical shortcomings, including the rarity and expense of ruthenium that limits its utilization in commercial applications.

Studies on solution-deposited thin films have shown that both the electronic (5) and protonic conductivity of hydrous RuO_2 are highly sensitive to both the crystallinity and hydroxyl content of the material (see Figure 1 which has been developed from literature reports) (5−13). As-deposited films tend to be amorphous, exhibit poor electron conductivity, and have both a high hydroxyl content and high proton conductivity. Heat treatments drive condensation reactions between hydroxyl groups, resulting in loss of water from the hydrous oxide, nucleation and growth of crystalline RuO_2 particles, and correspondingly, an increase in electronic conductivity, through rutile grains, and a decrease in protonic conduction, which is confined to path-

* Corresponding author. E-mail: mtbrumb@sandia.gov.
Received for review November 13, 2009 and accepted February 2, 2010
DOI: 10.1021/am9007903

Published on Web 02/11/2010

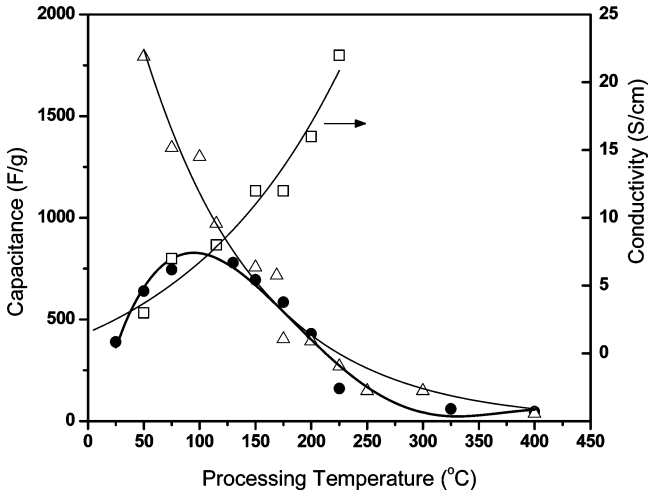

FIGURE 1. Gravimetric capacitance (dark circles) is plotted as a function of processing temperature for hydrous ruthenium oxide using data averaged from estimated literature values (5−13). A maximum capacitance is obtained at ca. 150 °C, where the water content is approximately $RuO_2 \cdot 0.5H_2O$. At low temperatures, the increase in capacitance correlates with the increase in electronic conductivity (open squares) estimated from data shown in ref 5. Capacitance decreases with increasing temperature above 150 °C, corresponding to grain growth of rutile RuO_2 and water loss. The decrease in water content (open triangles) is illustrated by weighting the theoretical value of capacitance for RuO_2, 1360 F/g, by the water content reported in refs 5−13 and normalized to the value obtained at 150 °C (i.e., 0.5). Lines are included as guides to the eye.

ways along hydroxyl groups at grain boundaries (6, 7). Empirically, it has been determined that the optimal performance for RuO_2 ultracapacitors occurs at a heat treatment of roughly 150 °C, corresponding to an approximate ratio of 1:2 H_2O:RuO_2, also referred to as hydrous RuO_2, Figure 1 (7). Under this processing condition, neither electronic nor protonic conduction is necessarily maximized, but both are cooperatively optimized to support pseudocapacitive behavior. Only a fraction of the RuO_2 is typically utilized giving a maximum capacitance, typically 700 to 800 F/g, only slightly greater than half the theoretical value, 1360 F/g (14, 15). Alternatively, a relatively routine fabrication process for preparing RuO_2 is through the thermal decomposition of $RuCl_3$. Anhydrous RuO_2 films are often prepared in this manner for use as the anodes in the electrolytic production of chlorine (3, 16−19). At the temperatures of the decomposition, between 300 and 500 °C, a highly electrically conducting crystalline RuO_2 is formed, whereas protonic conduction, which is low, is not as great a concern for this application.

The primary challenges associated with making ultracapacitors involve developing materials that are relatively easy and inexpensive to fabricate, yet provide suitable architectures to: (1) maximize electrolyte access, (2) minimize transport distances for both ions and electrons between the bulk and electrolyte surfaces, and (3) stabilize the material over numerous charge/discharge cycles and normal handling. Connectivity to the electrolyte is critically important and a high-surface-area, hierarchically porous nanostructure is desirable. Many attempts have been made to enhance the performance of RuO_2 electrodes including dilution of RuO_2 with other additives such as carbon (20−24), silica (14), and polymers (25−27), use of pre-existing templates such as anodized aluminum to make "nano-arrays" (28−35), and modification of the structures of layered clay-like ruthenates (36−39). These efforts clearly demonstrate that moving toward nanoarchitectures can push materials utilization and capacitance towards theoretical limits.

Despite the many demonstrations of nanostructured RuO_2 electrodes, few attempts to design RuO_2 with nanoscopic architecture through a surfactant templated approach are known to the authors (40). Here, we have attempted to exploit the formation of a ruthenium thiolate complex as a strategy for templated assembly of RuO_2. Ruthenium-thiolato complexes have been well-established, and the Ru−S linkage is known to be quite strong (41−47). Simple surfactant molecules represent an important class of templates, as these molecules can self-assemble to produce a wide range of mesophases in solution including micelles, inverse micelles, as well as extended lamellar, cubic, or hexagonal phases (48−50). For the classical case of silica, these extended phases have been shown to persist during the condensation reactions required to convert soluble silica precursors, such as alkoxides, into a condensed oxide phase replicating the template. Templating is effective for silica since the tetrahedral coordination geometry of silicon leads to the formation of random, amorphous structures amendable towards template replication (51, 52). However, most metal oxides contain octahedral metal centers that tend to crystallize during processing, where the crystallizing oxide imposes order on the relatively compliant surfactant phase. To circumvent this problem, metal−surfactant complexes have been prepared that can self-assemble into mesophases that persist through subsequent hydrolysis and condensation, thereby stabilizing the oxide architecture prior to removal of the surfactant (53, 54). The idea of "locking-in" an RuO_2 structure has been demonstrated in a related example where nanoscale porosity was introduced into RuO_2 using lanthanum in the preparation of the oxide (55). Lanthanum was then dissolved out of the RuO_2, leaving voids, and a high voltammetric charge was obtained with a peak in capacitance observed when 30% lanthanum was used in the precursor solution. A few other reports have also discussed the inhibition of RuO_2 densification and resulting capacitive increases (56, 57). In this work, RuO_2 particle coalescence is sterically inhibited via the complexed molecular template, leading to a hierarchical nanostructured oxide film.

For initial studies, we selected 1-hexanethiol as the specific surfactant molecule for complexation and templating functions. The template is sacrificial, and appears to be removed pyrollytically, leaving behind the desirable nanostructured RuO_2 in a one-step process. The electrochemical performance of the templated materials was significantly enhanced relative to untemplated RuO_2, and estimated gravimetric capacitances (see the Supporting Information) were very high considering the processing temperature. Extensive materials characterization reveals that the processing method appears to produce unique structures with nanoscale interconnectivity of small-scale ruthenium oxide

clusters formed via an initial steric inhibition of grain growth. The retention of such fine grained ruthenium oxide particles gives the highly electrically conducting oxide, which can be prepared only at high temperature, while maintaining a structure with a large internal surface area and a high degree of hydroxylation.

EXPERIMENTAL METHODS

Anhydrous 1-butanol and $RuCl_3 \cdot xH_2O$ were obtained from Acros. HCl, H_2SO_4, and deionized ultrafiltered water were obtained from Fisher. 1-Hexanethiol was obtained from Aldrich. All chemicals were used as received. Titanium (1.6 mm thick, 99.2%) was obtained from Alfa Aesar and was cut into square 1 cm^2 coupons to be used as substrates. Substrates were roughened with sand paper followed by brief exposure to KOH and subsequent sonication and rinsing in water followed by ethanol. Substrates were ozone plasma etched (UVOCS Inc.) for 5 min prior to $RuCl_3$ film deposition. Standard ruthenium chloride solutions consisted of 3 g of $RuCl_3 \cdot xH_2O$, 6.2 mL of 1-butanol, and 0.2 mL of concentrated HCl, following a modified procedure from the literature (3). 1-Hexanethiol additions were made on a relative molar basis to the Ru content in solution and are referred to according to those ratios, i.e., a 1:1 thiol:Ru sample had equivalent moles of 1-hexanethiol and $RuCl_3$ in the precursor solution, whereas 1:2 thiol:Ru had half as much thiol. For the sample shown in Figure 4A,B, $RuCl_3$ concentrations were 1/3 of that described above, because this more dilute condition most clearly illustrated the formation of circular nanofeatures. Film deposition was performed using a Laurell WS-400B-6NPP/LITE spin coater at 2000 rpm for 45 seconds. Samples were immediately removed from the spin coater and placed on a hot plate at 350 °C for 7 min in ambient atmosphere. Samples were cooled on a steel plate at room temperature under ambient conditions. The overall film thickness could be linearly increased by repeating the above process. Films discussed in this work comprise three layers, corresponding to approximately 1 μm total thickness. All procedures were performed in a fume hood. **Caution**: *Ruthenium chloride is extremely destructive to the respiratory system, butanol is flammable, and thiols are pungent and harmful.*

Powders were prepared via spallation of thick films of the ruthenium chloride solution upon heating in a glass petri dish at 350°C under ambient conditions in a fume hood. **Caution**: *Care must be taken to prevent spattering of chemicals during initial stages of solvent evolution*. After several seconds of heating, when most of the solvent had evaporated, the powders were gently crushed with a steel spatula to maintain good thermal contact with the petri dish. Characterization results from the powders were assumed to be transferable to the characteristics of the deposited thin films since the preparation conditions were nearly identical.

X-ray photoelectron spectroscopy (XPS) was performed with a Kratos Axis Ultra DLD with monochromatic Al Kα excitation (1486.6 eV). The analyzed spot size was 300 × 700 microns, and base pressures were $<5 \times 10^{-9}$ Torr. FIB-SEM cross-sections were performed using a FEI Helios NanoLab 600. TEM samples were prepared using a dual-beam focused ion beam/scanning electron microscope system as described above. TEM samples were characterized with a FEI Company Tecnai F30-ST scanning/transmission electron microscope (STEM) operated at 300 kV and equipped with an energy-dispersive x-ray spectrometer. Scanning electron microscopy work was completed on a Zeiss Supra 55 VP Field Emitter Gun (FEG) SEM. Images were collected using Zeiss SmartSEM software interface. The ^{1}H MAS NMR spectra were obtained on an Avance 600 instrument at 600.1 MHz using a 2.5 mm MAS probe. Spinning speeds were between 20 and 30 kHz utilizing a rotor synchronized Hahn echo. Chemical shifts were referenced to the secondary standard adamantane 1.38 ppm with respect to trimethylsilane (TMS). Deconvolutions and integration were performed using DMFIT software (58). Thermal analyses were performed using a Netzsch STA 409PC Luxx thermobalance for simultaneous TG-DTA.

Samples were heavily rinsed with water and ethanol and dried with nitrogen prior to use. The electrochemical performance of all films was evaluated in 1 M H_2SO_4. Electrochemistry was performed using a Princeton Applied Research PARSTAT 2273 potentiostat. A Pt mesh was used as the counter electrode for all measurements. Reference electrodes were either Hg/$HgSO_4$ (saturated K_2SO_4) or Ag/AgCl (3M KCl) as indicated in the figures. The working electrode was exposed to solution through a circular 0.1 cm^2 opening at the bottom of a Teflon well sealed with a Teflon-coated silicone o-ring.

Further details on experimental methods are given in the Supporting Information.

RESULTS

Electrochemical Characteristics. The cyclic voltammetry data for the untemplated RuO_2 film are shown in Figure 2A, with a low overall capacitance and redox peaks as have been previously observed (3, 59−62). However, the data from the templated RuO_2 materials are unusual for thermally prepared RuO_2. Typical voltammograms show that the templated RuO_2 films generated currents 4 times greater than untemplated-RuO_2 films, Figure 2B,C relative to Figure 2A. In addition, the voltammetric shapes changed from that of untemplated-RuO_2, which exhibited resolvable redox peaks, to broad "squarish" voltammograms without any resolvable peaks, similar to that obtained for hydrous ruthenium oxide and mixed oxide systems (2, 5−7, 12). The higher currents for the templated materials imply greater utilization and access of the electrolyte to the RuO_2 material. For all cases, the capacitance decreased with increasing sweep rate as has been previously observed and discussed for ruthenium and other oxide systems, Figure 3 (14, 23, 29, 63). However, the rate of capacitance decay with sweep rate was slower, up to 100 mV/s, for the templated materials, suggesting mitigation of loss processes in the templated films (3, 62−64).

Normalization of the currents to sample mass has not been performed in this work since the sample masses were estimated to be approximately the same for each material analyzed. The mass of deposited material could be estimated using the density (6.97 g/cm^3 for RuO_2) and electrochemically analyzed volume, determined from the exposed area (a circular ca. 0.1 cm^2) and the film thickness. Film thicknesses were found to be very consistent between samples and among the various layers of a given sample (approximately 300 nm per layer, see the Supporting Information). A correction for porosity was not made, and consequently, estimated gravimetric capacitances are likely to be underestimations. The underestimation may be more significant for films derived from thiol-containing solutions where greater porosity was evident via SEM and TEM. Direct gravimetric weighing of the deposited films was determined to be inadequate for reliably measuring the deposited film mass and was susceptible to many sources of error. Using

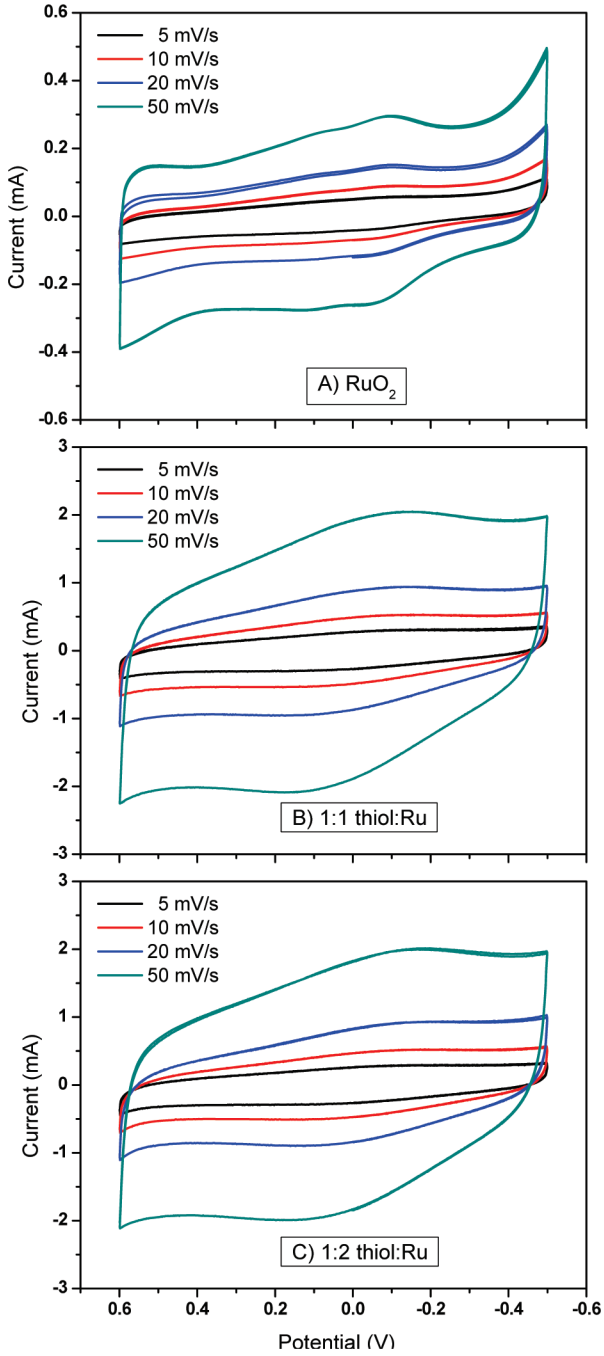

FIGURE 2. Cyclic voltammetry of ruthenium oxide thin films on titanium are shown for (A) thermally prepared RuO_2, and RuO_2 formed with (B) 1:1 and (C) 1:2 molar additions of thiol relative to Ru in the precursor solution. The electrolyte solution was 1 M H_2SO_4 and potentials are referenced to $Hg/HgSO_4$. Three voltammograms are shown for each scan rate. Scan rates were 5 (black), 10 (red), 20 (blue), and 50 (green) mV/s.

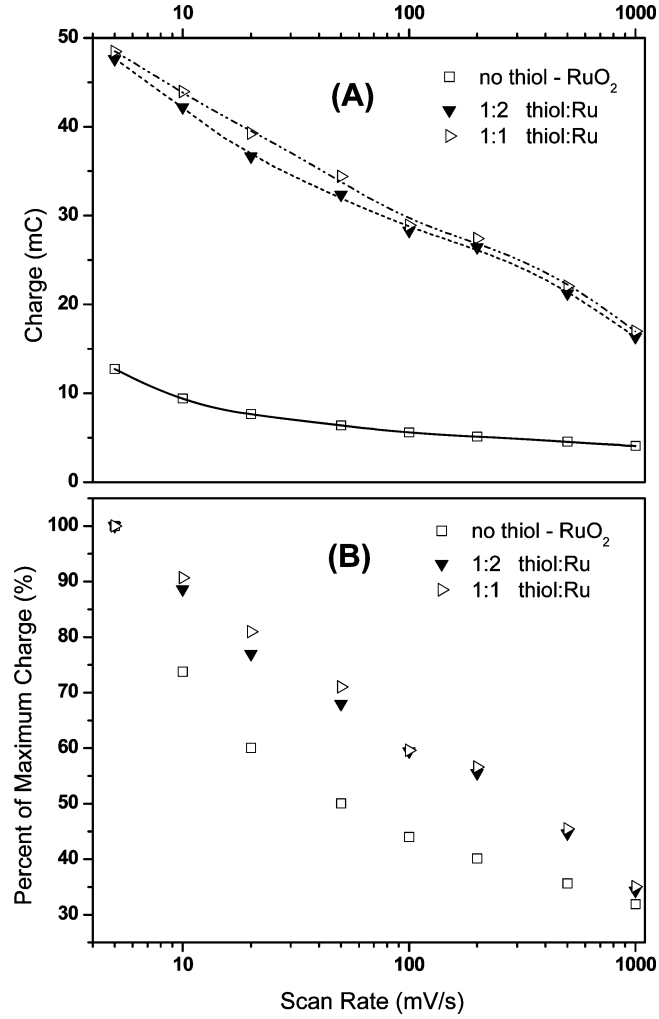

FIGURE 3. (A) Voltammetric charge from the cathodic scan (cyclic voltammetry in Figure 2) is shown as a function of scan rate for the untemplated and templated RuO_2 films. (B) The charge is normalized to the maximum value obtained for each respective film, showing that the decay in coulometric charge with scan rate is much faster for the untemplated RuO_2 relative to templated RuO_2.

the estimations, the gravimetric capacitance for untemplated RuO_2 would be ca. 200 F/g, comparable to values reported in literature for other anhydrous-type RuO_2 materials. For the templated materials, the gravimetric capacitances would be estimated near 400−500 F/g. Such values are exceptionally high for thermally processed ruthenium oxide, where the RuO_2 would be expected to be anhydrous, and are approaching benchmark values reported for hydrous ruthenium oxide, ca. 760 F/g (2). This unusual observation of achievable high gravimetric capacitances with RuO_2, prepared under conditions where it ought to be anhydrous, was further investigated by characterization of the templated and untemplated materials.

Microscopy. RuO_2 prepared via thermal decomposition of $RuCl_3$ is known to be somewhat porous (3), although most of the porosity was found here to reside near the film-substrate interface (see Figure SI1 in the Supporting Information). The porosity appears to be a result of inefficient compaction of RuO_2 rutile crystallites. X-ray diffraction (XRD) confirms rutile RuO_2 for the untemplated films (see Figure SI2 in the Supporting Information). Higher processing temperatures or continued annealing lead to larger RuO_2 crystallites and densification of the film. Alternatively, the porosity in the templated RuO_2 samples appears to be hierarchical. SEM images of the templated films show a regular array of circular features, 300 ± 50 nm in diameter, at the surface of the templated RuO_2, Figure 4A−C. Lower concentrations of $RuCl_3$ in the precursor solution cause a higher density of the circular features as shown in Figure

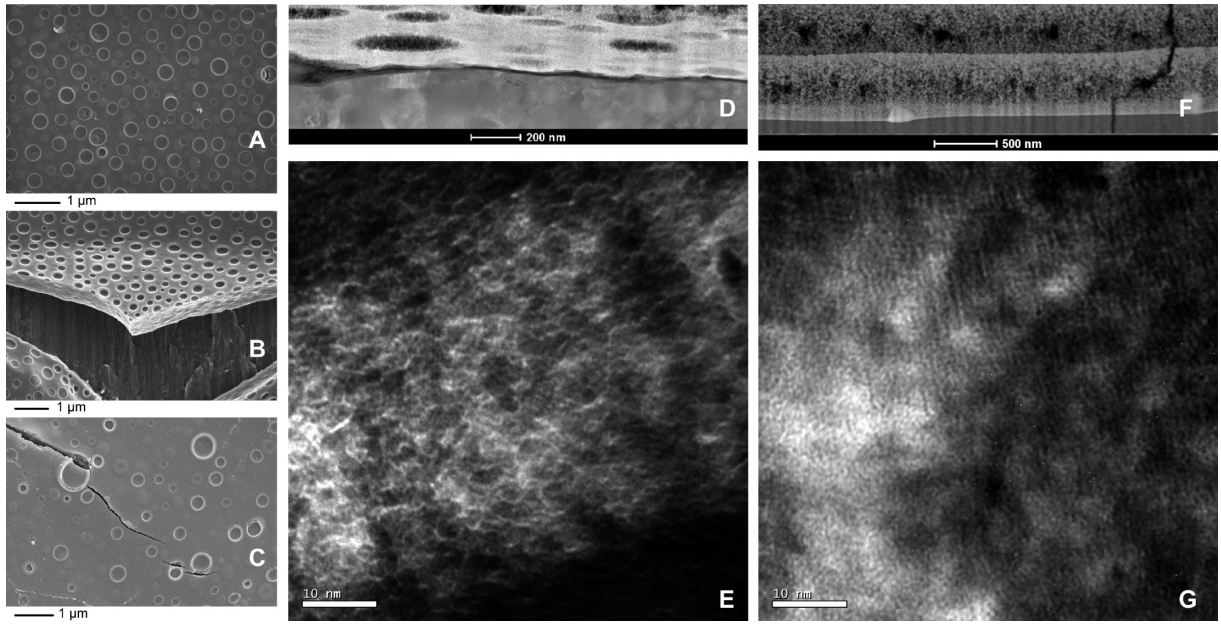

FIGURE 4. (A−C) Topographical SEM images of templated ruthenium oxide. A regular array of circular features is evident. Subsurface porosity from the gas bubble evolution can be observed in the cross-sectional fragment in B as well as in the TEM cross-section D of the RuO_x film on titanium. (D) Cross-sectional TEM of the templated ruthenium oxide shows lenticular pores that at (E) higher magnification are composed of an interwoven, fine grained material and nanoscopic porosity. (F, G) TEM cross-sections of untemplated RuO_x are shown for comparison.

4A,B. The circular features appear to exist subsurface as pores, as illustrated in Figure 4B, where part of the film has pealed back from the titanium surface. These features were not observed for untemplated-RuO_2 and are likely a result of bubble generation and gas evolution from pyrolysis of the templating material. In addition to the 300 nm pores observed via SEM, there is an open network of extremely small, ill-defined pores (on the order of 4 nm in diameter), defined by primary RuO_2 particles ca. 0.5 nm in diameter observed via TEM (Figure 4D and Figure 4E). XRD does not show a rutile diffraction pattern for the templated materials (see Figure SI2 in the Supporting Information), possibly because of the very fine grained RuO_2 in the templated films. At no length scale was there evidence for the formation of an ordered mesophase, indicating the template did not self-assemble into micelles or other features such as those reported for the Nb_2O_5 system (54); however, the hierarchical porosity is advantageous for electrolyte percolation through the film and is desirable for optimizing electrochemical capacitance. We suspect the chain length of hexane thiol is too short to support formation of a mesophase; however, it is clearly impacting the growth of rutile RuO_2 grains and leads to a hierarchically porous, nanostructured film.

Materials Characterization. As discussed above, the hydroxyl content of hydrous ruthenium oxide is critical to its pseudocapacitive behavior. We have determined the hydroxyl content of our materials using a combination of thermogravimetric analyses (TGA, see the Supporting Information) (65−69), infrared spectroscopy (IR), and solid-state proton (^{1}H) magic angle spinning (MAS) NMR spectroscopy. There have been a limited number of solid state NMR studies of hydrous RuO_x (70−72). These studies include both static ^{1}H and ^{2}H investigations that show a correlation between the water dynamics and the observed conductivity in the hydrous RuO_x. Here, the proton intensity is assumed to be predominantly associated with hydroxyl-type species in the RuO_x material. The hydroxyl content of the baseline material is low, approximately 1:10 OH:Ru, and is consistent with literature values for materials heated to 350°C (see Figure 1). The XRD analysis of untemplated RuO_2, confirming rutile RuO_2, is consistent with particle diameters of approximately 9 nm (based on estimations from the peak widths,see Figure SI2A in the Supporting Information). The hydroxyl content of bulk rutile RuO_2 is negligible, with nearly all of the hydroxyl groups residing on particle surfaces (73−76). On the basis of the density of rutile RuO_2 (6.97 g/cm^3) and assuming non-contacting 9 nm spherical particles, the net calculated OH:Ru ratio would be approximately 1:5. The discrepancy between the experimental and theoretical ratios is likely due to condensation reactions between particles in a real material, which would eliminate a significant fraction of surface hydroxyl groups. Nevertheless, the hydroxyl contents for the templated RuO_2 materials are significantly higher than for the baseline RuO_2, i.e., proton intensities in NMR are nearly 30 times greater than that of the baseline material. The NMR results, Figure 5, and XPS results, Figure 6, are described in detail below characterizing both the concentration and local molecular geometry of hydroxyl groups in the structure.

The NMR spectra reveal that there are two distinct types of hydroxyl groups. Identification of the hydroxyl groups is estimated by considering the formal charge on the ruthenium, the expected 6-fold coordination on the ruthenium, the subsequent partial charge on the surrounding oxygens, and the corresponding effective charge on the hydrogen. In general, the NMR spectra can be interpreted where environments of greater acidity are observed at more positive chemical shifts, similar to that observed in niobium oxide

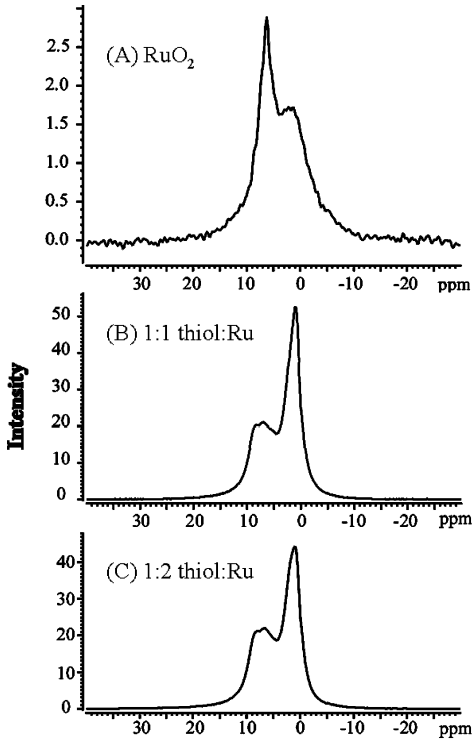

FIGURE 5. ^{1}H MAS NMR of ruthenium oxide powders illustrate large differences in the hydroxyl content and distribution in the (A) untemplated ruthenium oxide material versus ruthenium oxide prepared with thiol additives at (B) 1:1 thiol:Ru and (C) 1:2 thiol:Ru.

(77). In addition, the present hydroxyl assignment is based on chemical shift assignments for NbOH ($\delta \approx 1-2$ ppm) (77, 78), ZrOH ($\delta \approx 2.4-4.8$ ppm) (79), and TiOH ($\delta \approx 1.3$ ppm) (80). We therefore associate the peak at chemical shift near 2.5 ppm with terminal (nonbridging) hydroxyls, whereas the peak near 6.5 ppm is associated with hydroxyl groups bridging two Ru centers (see Figure 7). In the baseline material (Figure 5A), the ratio of peak areas for bridging to terminal (nonbridging) hydroxyls is 4:3. The experimental bridging:nonbridging ratio is slightly higher than the 1:1 ratio that would be expected from the surface stoichiometry of the crystalline rutile structure, probably because of some residual hydrogen bonded water species (75, 76). Conversion of some terminal hydroxyls to bridging hydroxyls at particle contacts may also lead to some discrepancy between the experimental value and the theoretical value.

In addition to the high hydroxyl content observed for the templated materials, particularly in comparison to other RuO_2 materials heated to 350 °C (Figure 1), the templated materials also exhibit an excess of non-bridging groups relative to bridging hydroxyl groups (Figure 5). From Figure 5B,C, the ratios of bridging:nonbridging hydroxyls were 1:2 and 2:3 for the 1:1 thiol:Ru and 1:2 thiol:Ru materials, respectively. The unusually high OH:Ru content, and the larger-than-expected bridging:nonbridging hydroxyl ratios for the template materials, suggest a metal oxide architecture with small grain sizes such that there is high internal surface area available for hydroxylation.

XPS data are shown (Figure 6) for the O (1s) core levels of the untemplated-RuO_x and templated-RuO_x materials

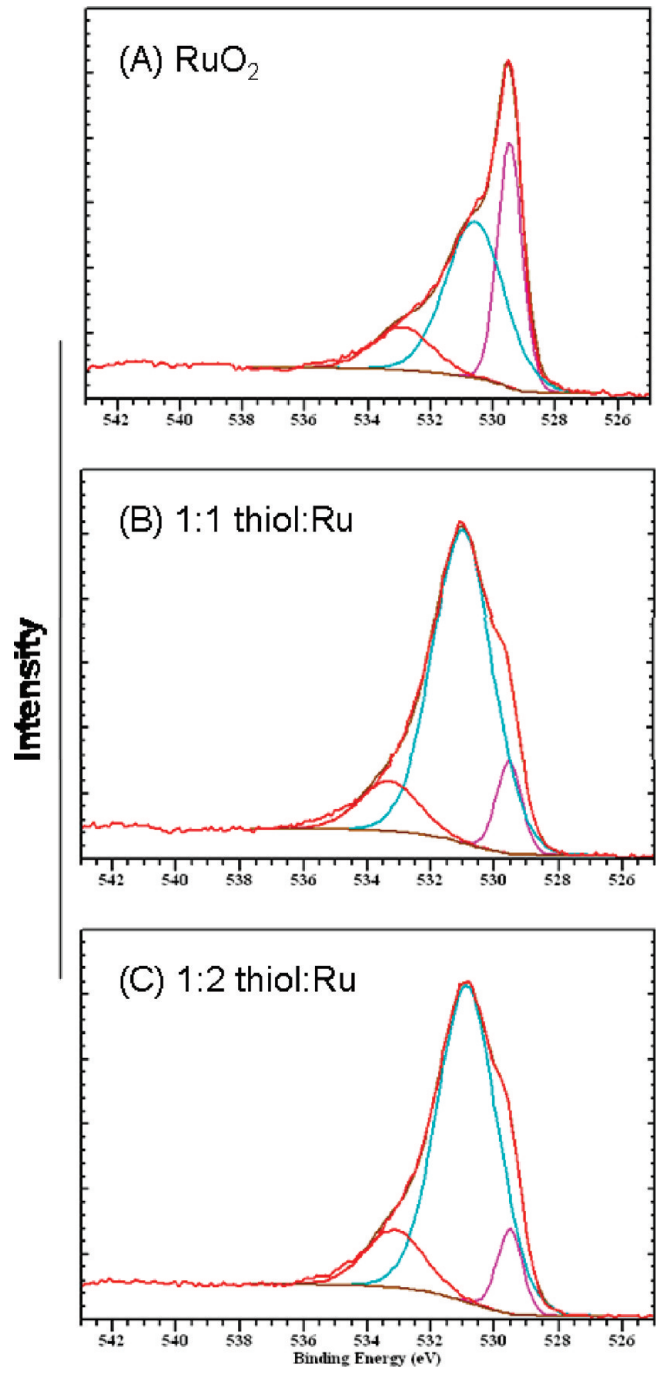

FIGURE 6. XPS spectra showing the O (1s) core level for (A) untemplated-RuO_x, (B) 1:1 thiol:Ru templated-RuO_x, and (C) 1:2 thiol:Ru templated-RuO_x. Identical synthetic components can be used to fit each spectrum with only minor shifts in the peak positions. The spectra indicate a much higher percentage of hydroxide species in the templated materials relative to untemplated-RuO_x.

confirming the NMR results and higher hydroxyl content in the templated materials. A Shirley background was used and O (1s) components (Gaussian/Lorentzian GL(30)) were restricted to FWHM of 0.93, 2.2, and 2.2 for the first, second, and third components, respectively, for all samples. Table 1 summarizes the peak positions and relative area of the fitted components. Kim et. al. have determined the binding energies for various ruthenium oxide species showing that the first component, at ca. 529.5 eV, is oxygen in the RuO_2

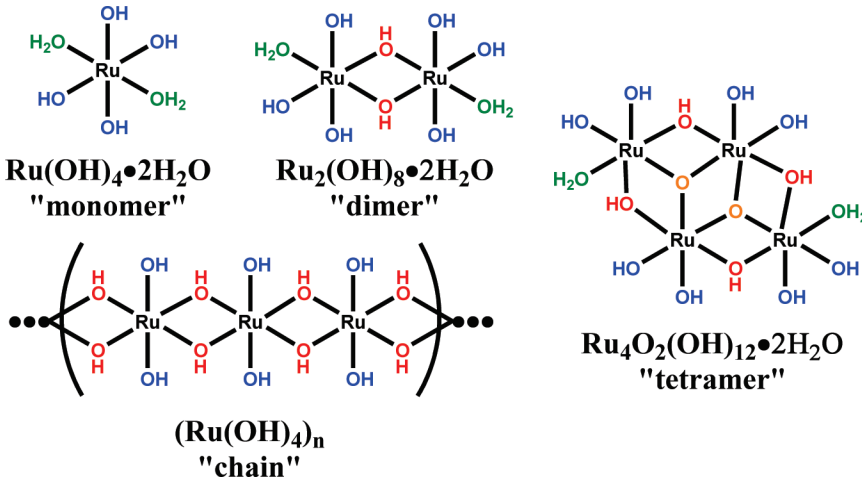

FIGURE 7. Relative ratios of bridging (red) to nonbridging (blue) hydroxyls is illustrated as a function of ruthenium cluster size. For a fully hydroxylated single ruthenium (i.e., "monomer") there are effectively six terminal hydroxyl environments and no bridging hydroxyls, and the ratio of hydroxyls to ruthenium is at its maximum, 6:1 OH_x:Ru. However, as cluster size increases, the ratio of bridging:nonbridging approaches unity and the ratio of hydroxyls:Ru rapidly decreases.

Table 1. XPS Fitting Components of the O (1s) core level for Untemplated RuO_x and Templated RuO_x

	1st component	2nd component	3rd component
	peak positions		
untemplated-RuO_x	529.47	530.58	532.91
1:1 thiol:Ru	529.55	531.00	533.32
1:2 thiol:Ru	529.53	530.87	533.15
	peak areas		
untemplated-RuO_x	34.1	51.6	14.3
1:1 thiol:Ru	9.7	77.8	12.4
1:2 thiol:Ru	8.7	77.1	14.1

oxide (81). Components at higher binding energies are associated with hydroxides. It is clearly evident from XPS that hydroxides are present at significantly higher concentrations in the templated RuO_x materials, as was observed via NMR. Additionally, data from depth profile time of flight secondary ion mass spectrometry (TOF-SIMS) (see Table SII in the Supporting Information) corroborates the observations discussed above where intensities from RuO and O fragments were quite similar between samples, but higher hydroxyl intensities were observed for the templated material. The NMR and XPS data clearly show that the templated RuO_2 films retain a hydrous-like character despite the high-temperature processing that would otherwise be expected to produce anhydrous RuO_2.

DISCUSSION

The culmination of NMR, XPS, and XRD data indicating high hydroxyl concentrations, high bridging-to-nonbridging hydroxyl ratios, and nanoscale particle sizes suggest an oxide structure dissimilar from that of typical rutile RuO_2. As observed via SEM and TEM, the characterization results illustrate that the templated RuO_2 consists of an interconnected network of molecular clusters where the area available for hydroxylation is significantly enhanced. Our speculation is that crystallization of rutile RuO_2 is prevented via an induced steric hindrance of the thiol template. For the baseline case of untemplated ruthenium oxide, heating leads to conversion and condensation of the complex mixture of $Ru_aCl_xOH_y(H_2O)_z$ monomers, dimers, etc., resulting in RuO_2 grains with evolution of Cl_2. Figures 7 and 8 are schematics illustrating possible ruthenium species where Cl and OH could be replaced interchangeably depending on whether the cluster is the precursor material or the thermally oxidized material that has subsequently hydroxylated/hydrated from ambient exposure. Following conversion to RuO_2, subsequent crystalline grain growth of RuO_2 would be dependent on time and temperature for the baseline case. However, for the templated RuO_2 materials, the initial solution precursors are appended by hexanethiol groups via Ru—S bonds. As with the baseline case, initial heating results in condensation reactions to produce RuO_2; however, the hexyl groups sterically hinder further condensation, Figure 8. The resulting structure is a locked-in, interconnected network of RuO_xOH_y clusters that apparently do not further densify upon eventual pyrolysis of the template. Such a structure, and mechanism, is consistent with the NMR results where hydroxyl content and nonbridging hydroxyls would be expected to be higher than for large-grain RuO_2.

The above results can be used to infer limits on the characteristics of cluster networks in the templated ruthenium oxide materials. In the discussion of such models, it is assumed that each Ru^{IV} is octahedrally coordinated to six oxygens, whereas each oxygen can be bound to either one (a non-bridging hydroxyl or water molecule), two (a bridging hydroxyl or oxo-bridge), or three ruthenium atoms (a tri-bridging oxygen). Proton content is adjusted to maintain charge neutrality, and coordinated water is regarded as a terminal hydroxyl. Within these constraints, models were developed to determine the OH:Ru and bridging-OH:nonbridging-OH hydroxyl ratios. As shown in Figure 7, the progression from the monomeric hydroxide $(Ru(OH)_4 \cdot 2H_2O)$ to the edge-shared dimer $(Ru(OH)_4 \cdot H_2O)_2$,

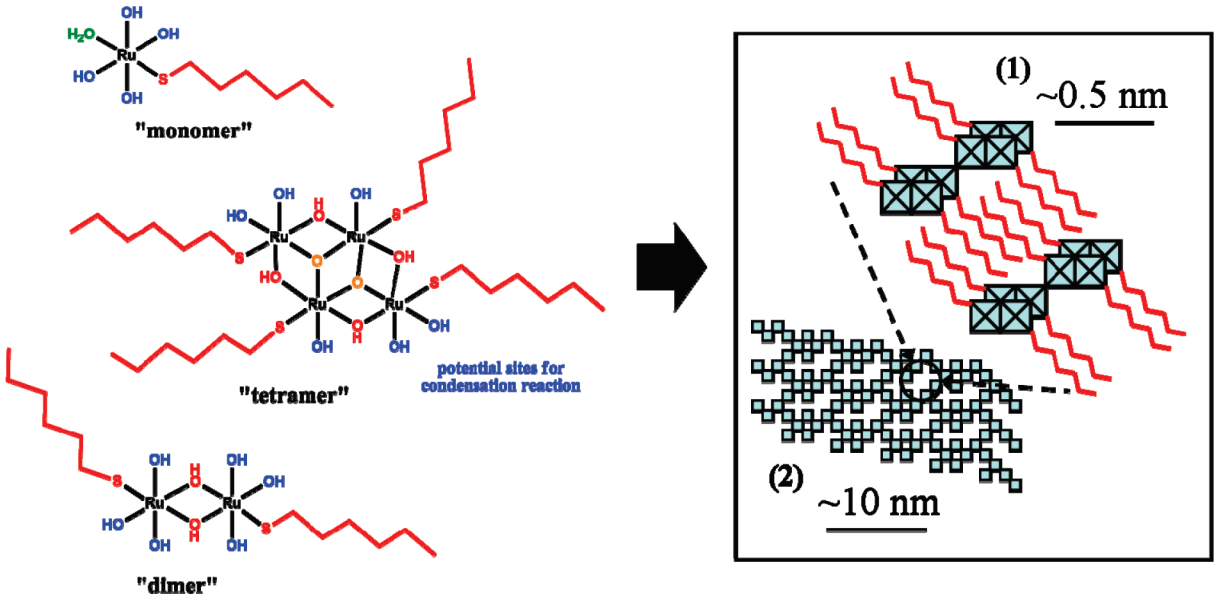

FIGURE 8. Use of a thiol templating agent, which coordinates directly to Ru through a Ru−S bond, sterically hinders condensation and formation of large grained rutile RuO_2. Small clusters of RuO_xOH_y are able to condense as shown in (1); however, the alkyl groups prevent the clusters from coming into proximity with one another, leading to condensation at only a limited number of contact points. The resulting structure is an interweaving network of very fine grained, hydroxylated ruthenium oxide as illustrated in (2).

to infinite chains of edge shared octahedral $(Ru(OH)_4)_n$ is shown. In this progression, the OH:Ru ratio changes from 6:1 to 5:1 to 4:1. The bridging-OH:nonbridging-OH ratio changes from 0:6 to 1:4 to 1:1. This example illustrates that as the "degree of condensation" increases, i.e., as grain size increases, there is a corresponding decrease in OH:Ru and an increase in the bridging-OH:nonbridging-OH ratio. Lower hydroxyl content and lower nonbridging-OH concentrations both detrimentally affect proton conductivity in RuO_2; however, increased rutile grain size positively impacts electrical conductivity.

We propose that the best model to explain the observed characterization data is an oxide structure of an extended network of basic building blocks of double-chain tetramers. The isolated tetrameric unit $(Ru_4O_2(OH)_{12} \cdot 2H_2O)$ would have OH:Ru = 14:4 and bridging−OH:nonbridging−OH = 2:5. A continuous network of these tetrameric units would have similar OH:Ru ratios; however, the bridging−OH: nonbridging−OH ratios could be altered depending on whether tetrameric units were linked via corner-sharing Ru−O−Ru or edge sharing Ru-2O−Ru bonds (as illustrated for the "chain" species). Regardless, these ratios are comparable to those observed via NMR for the templated RuO_2 materials (OH:Ru = 3:1 and bridging-OH:nonbridging-OH from 1:2 to 2:3). The tetrameric cluster size inferred from the NMR results is comparable to the "primary particle size" observed via TEM measurements, around 0.5 nm. This type of network structure explains the electrochemical performance observed in Figures 2 and 3, where greater utilization of ruthenium for charge storage was observed because the cluster size is small enough for most ruthenium to be electroactive, and utilization of material was obtained at higher scan rates because of good electrolyte access and continuous electrical and proton conducting networks.

CONCLUSIONS

Stabilization of the RuO_2 as a network of nano-ruthenate clusters has been explored as an advantageous strategy for producing pseudocapacitve electrodes since nearly every Ru site is in near-surface proximity and is potentially available for redox activity. Hierarchical porosity formed from the sacrificial template leads to facile electrolyte access, while protonic and electronic conduction are preserved through the network of hydroxylated RuO_2 nanograins. We are in the process of modeling electrochemical data to extract quantitative values for parameters such as proton diffusion to further rationalize performance. In addition, these models are being used to predict the behavior of molecular cluster architectures and establish the potential rate limiting steps including electron, proton, and electrolyte transport as related to cluster size and connectivity. Studies on ion exchange in zeolites and recent work on nanoporous carbons have shown unexpected behavior as pore sizes have been reduced to near that of the solvated ions (82−85). We believe that the use of templates to stabilize molecular cluster architectures represents a significant advance in the development of materials for ultracapacitors and future work is exploring the extent to which this strategy can be applied to less expensive electrochemically active oxides.

Acknowledgment. Thanks to Michael Rye and Garry Bryant for FIB-SEM cross-section analyses, Terry Garino for help with thermal analyses, James (Tony) Ohlhausen for TOF-SIMS analyses, and Ralph G. Tissot for XRD analyses. Thanks also to Erik Spoerke, Robert Nilson, Mark Roberts, Dave Wheeler, and Geoff Brennecka for thoughtful discussions. The authors are grateful for support from Sandia National Laboratories Laboratory Directed Research and Development Program. Sandia is a multiprogram laboratory

operated by Sandia Corporation, a Lockheed Martin Company, for the United States Department of Energy's National Nuclear Security Administration under Contract DE-AC04-94AL85000.

Supporting Information Available: Cross-sectional SEM images of ruthenium oxide layers, XRD from RuO_2 powders, additional ^1H MAS NMR spectra, FTIR of RuO_2 powders, XPS survey spectra, TGA, and depth profile data from TOF-SIMS (PDF). This material is available free of charge via the Internet at http://pubs.acs.org.

REFERENCES AND NOTES

(1) Kotz, R.; Carlen, M. *Electrochim. Acta* **2000**, *45*, 2483.
(2) Zheng, J. P.; Cygan, P. J.; Jow, T. R. *J. Electrochem. Soc.* **1995**, *142*, 2699.
(3) Conway, B. *Electrochemical Supercapacitors: Scientific Fundamentals and Technological Applications*; Kluwer Academic: New York, 1999.
(4) Zheng, J. P.; Huang, J.; Jow, T. R. *J. Electrochem. Soc.* **1997**, *144*, 2026.
(5) Barbieri, O.; Hahn, M.; Foelske, A.; Kotz, R. *J. Electrochem. Soc.* **2006**, *153*, A2049.
(6) Dmowski, W.; Egami, T.; Swider-Lyons, K. E.; Love, C. T.; Rolison, D. R. *J. Phys. Chem. B* **2002**, *106*, 12677.
(7) McKeown, D. A.; Hagans, P. L.; Carette, L. P. L.; Russell, A. E.; Swider, K. E.; Rolison, D. R. *J. Phys. Chem. B* **1999**, *103*, 4825.
(8) Rolison, D. R.; Hagans, P. L.; Swider, K. E.; Long, J. W. *Langmuir* **1999**, *15*, 774.
(9) Long, J. W.; Swider, K. E.; Merzbacher, C. I.; Rolison, D. R. *Langmuir* **1999**, *15*, 780.
(10) Foelske, A.; Barbieri, O.; Hahn, M.; Kotz, R. *Electrochem. Solid-State Lett.* **2006**, *9*, A268.
(11) Fang, Q. L.; Evans, D. A.; Roberson, S. L.; Zheng, J. P. *J. Electrochem. Soc.* **2001**, *148*, A833.
(12) Kim, I. H.; Kim, K. B. *J. Electrochem. Soc.* **2006**, *153*, A383.
(13) Chang, K. H.; Hu, C. C.; Chou, C. Y. *Chem. Mater.* **2007**, *19*, 2112.
(14) Min, M.; Machida, K.; Jang, J. H.; Naoi, K. *J. Electrochem. Soc.* **2006**, *153*, A334.
(15) Hu, C. C.; Chen, W. C.; Chang, K. H. *J. Electrochem. Soc.* **2004**, *151*, A281.
(16) Barison, S.; Daolio, S.; Fabrizio, M.; De Battisti, A. *Rapid Commun. Mass Spectrom.* **2004**, *18*, 278.
(17) Forti, J. C.; Olivi, P.; de Andrade, A. R. *Electrochim. Acta* **2001**, *47*, 913.
(18) Roginskaya, Y. E.; Morozova, O. V. *Electrochim. Acta* **1995**, *40*, 817.
(19) Trasatti, S. *Electrochim. Acta* **2000**, *45*, 2377.
(20) Lin, C.; Ritter, J. A.; Popov, B. N. *J. Electrochem. Soc.* **1999**, *146*, 3155.
(21) Lee, J. K.; Pathan, H. M.; Jung, K. D.; Joo, O. S. *J. Power Sources* **2006**, *159*, 1527.
(22) Ramani, M.; Haran, B. S.; White, R. E.; Popov, B. N.; Arsov, L. *J. Power Sources* **2001**, *93*, 209.
(23) Zheng, J. P. *Electrochem. Solid-State Lett.* **1999**, *2*, 359.
(24) Barranco, V.; Pico, F.; Ibañez, J.; Lillo-Rodenas, M. A.; Linares-Solano, A.; Kimura, M.; Oya, A.; Rojas, R. M.; Amarilla, J. M.; Rojo, J. M. *Electrochim. Acta* **2009**, *54*, 7452.
(25) Song, R. Y.; Park, J. H.; Sivakkumar, S. R.; Kim, S. H.; Ko, J. M.; Park, D. Y.; Jo, S. M.; Kim, D. Y. *J. Power Sources* **2007**, *166*, 297.
(26) Huang, L. M.; Wen, T. C.; Gopalan, A. *Electrochim. Acta* **2006**, *51*, 3469.
(27) Hong, J. I.; Yeo, I. H.; Paik, W. K. *J. Electrochem. Soc.* **2001**, *148*, A156.
(28) Susanti, D.; Tsai, D. S.; Huang, Y. S.; Korotcov, A.; Chung, W. H. *J. Phys. Chem. C* **2007**, *111*, 9530.
(29) Hu, C. C.; Chang, K. H.; Lin, M. C.; Wu, Y. T. *Nano Lett.* **2006**, *6*, 2690.
(30) Tan, H.; Ye, E. Y.; Fan, W. Y. *Adv. Mater.* **2006**, *18*, 619.
(31) Cross, M. W.; Varhue, W. J.; Hitt, D. L.; Adams, E. *Nanotech.* **2008**, 19.
(32) Chu, S. Z.; Wada, K.; Inoue, S.; Hishita, S.; Kurashima, K. *J. Phys. Chem. B* **2003**, *107*, 10180.
(33) Chu, S. Z.; Inoue, S.; Wada, K.; Hishita, S. *J. Electrochem. Soc.* **2004**, *151*, C38.
(34) Subhramannia, M.; Balan, B. K.; Sathe, B. R.; Mulla, I. S.; Pillai, V. K. *J. Phys. Chem. C* **2007**, *111*, 16593.
(35) Lee, D. J.; Yim, S. S.; Kim, K. S.; Kim, S. H.; Kim, K. B. *Electrochem. Solid-State Lett.* **2008**, *11*, K61.
(36) Sugimoto, W.; Iwata, H.; Murakami, Y.; Takasu, Y. *J. Electrochem. Soc.* **2004**, *151*, A1181.
(37) Sugimoto, W.; Iwata, H.; Yokoshima, K.; Murakami, Y.; Takasu, Y. *J. Phys. Chem. B* **2005**, *109*, 7330.
(38) Sugimoto, W.; Saida, T.; Takasu, Y. *Electrochem. Commun.* **2006**, *8*, 411.
(39) Sugimoto, W.; Iwata, H.; Yasunaga, Y.; Murakami, Y.; Takasu, Y. *Angew. Chem., Int. Ed.* **2003**, *42*, 4092.
(40) Lin, K. M.; Chang, K. H.; Hu, C. C.; Li, Y. Y. *Electrochim. Acta* **2009**, *54*, 4574.
(41) Belchem, G.; Steed, J. W.; Tocher, D. A. *J. Chem. Soc., Dalton Trans.* **1994**, 1949.
(42) Jessop, P. G.; James, B. R. *Inorg. Chim. Acta* **1998**, *280*, 75.
(43) Jessop, P. G.; Rettig, S. J.; Lee, C. L.; James, B. R. *Inorg. Chem.* **1991**, *30*, 4617.
(44) Evans, I. P.; Spencer, A.; Wilkinso, G. *J. Chem. Soc., Dalton Trans.* **1973**, 204.
(45) Matsui, H.; Kawahara, T.; Kajita, H.; Seguchi, Y.; Yoshihara, M. *J. Mater. Sci.* **2006**, *41*, 7302.
(46) Povse, V. G.; Olabe, J. A. *Transition Met. Chem.* **1998**, *23*, 657.
(47) Tsukatani, T.; Fujihara, H. *Langmuir* **2005**, *21*, 12093.
(48) Firouzi, A.; Stucky, G. D.; Chmelka, B. F. *Synth. Porous Mater.* **1997**, *69*, 379.
(49) Huo, Q. S.; Margolese, D. I.; Ciesla, U.; Feng, P. Y.; Gier, T. E.; Sieger, P.; Leon, R.; Petroff, P. M.; Schuth, F.; Stucky, G. D. *Nature* **1994**, *368*, 317.
(50) Zhao, D. Y.; Feng, J. L.; Huo, Q. S.; Melosh, N.; Fredrickson, G. H.; Chmelka, B. F.; Stucky, G. D. *Science* **1998**, *279*, 548.
(51) Beck, J. S.; Vartuli, J. C.; Roth, W. J.; Leonowicz, M. E.; Kresge, C. T.; Schmitt, K. D.; Chu, C. T. W.; Olson, D. H.; Sheppard, E. W.; Mccullen, S. B.; Higgins, J. B.; Schlenker, J. L. *J. Am. Chem. Soc.* **1992**, *114*, 10834.
(52) Kresge, C. T.; Leonowicz, M. E.; Roth, W. J.; Vartuli, J. C.; Beck, J. S. *Nature* **1992**, *359*, 710.
(53) Antonelli, D. M. *Microporous Mesoporous Mater.* **1999**, *33*, 209.
(54) Antonelli, D. M.; Nakahira, A.; Ying, J. Y. *Inorg. Chem.* **1996**, *35*, 3126.
(55) Murakami, Y.; Kondo, T.; Shimoda, Y.; Kaji, H.; Zhang, X. G.; Takasu, Y. *J. Alloys Compd.* **1997**, *261*, 176.
(56) Chang, K. H.; Hu, C. C. *Appl. Phys. Lett.* **2006**, *88*.
(57) Tyrlik, S. K.; Kurzak, K.; Randzio, S. L. *Transition Met. Chem.* **1995**, *20*, 330.
(58) Massiot, D.; Fayon, F.; Capron, M.; King, I.; Le Calve, S.; Alonso, B.; Durand, J.-O.; Bujoli, B.; Gan, Z.; Hoatson, G. *Magn. Reson. Chem.* **2002**, *40*, 70.
(59) Arikado, T.; Iwakura, C.; Tamura, H. *Electrochim. Acta* **1977**, *22*, 513.
(60) Fachinotti, E.; Guerrini, E.; Tavares, A. C.; Trasatti, S. *J. Electroanal. Chem.* **2007**, *600*, 103.
(61) Galizzio, D.; Tantardi, F.; Trasatti, S. *J. Appl. Electrochem.* **1974**, *4*, 57.
(62) Ardizzone, S.; Fregonara, G.; Trasatti, S. *Electrochim. Acta* **1990**, *35*, 263.
(63) Doubova, L. M.; Daolio, S.; De Battisti, A. *J. Electroanal. Chem.* **2002**, *532*, 25.
(64) Onuchukwu, A. I.; Trasatti, S. *J. Appl. Electrochem.* **1991**, *21*, 858.
(65) Watanabe, H.; Utsuyama, H.; Sahara, S. *Chem. Lett.* **1990**, 1391.
(66) Newkirk, A. E.; Mckee, D. W. *J. Catal.* **1968**, *11*, 370.
(67) Vazquez-Gomez, L.; Horvath, E.; Kristof, J.; De Battisti, A. *Thin Solid Films* **2006**, *515*, 1819.
(68) Kristof, J.; Szilagyi, T.; Horvath, E.; Frost, R. L. *Thin Solid Films* **2005**, *485*, 90.
(69) Comninellis, C.; Vercesi, G. P. *J. Appl. Electrochem.* **1991**, *21*, 136.
(70) Fu, R.; Ma, Z.; Zheng, J. P. *J. Phys. Chem. B* **2002**, *106*, 3592.
(71) Ma, Z.; Zheng, J. P.; Fu, R. *Chem. Phys. Lett.* **2000**, *331*, 64.
(72) Zheng, J. P. *Electrochem. Soc. Trans.* **2008**, *6*, 147.
(73) Lister, T. E.; Chu, Y.; Cullen, W.; You, H.; Yonco, R. M.; Mitchell, J. F.; Nagy, Z. *J. Electroanal. Chem.* **2002**, *524*, 201.
(74) Chu, Y. S.; Lister, T. E.; Cullen, W. G.; You, H.; Nagy, Z. *Phys. Rev. Lett.* **2001**, *86*, 3364.
(75) Kim, Y. D.; Seitsonen, A. P.; Wendt, S.; Wang, J.; Fan, C.; Jacobi, K.; Over, H.; Ertl, G. *J. Phys. Chem. B* **2001**, *105*, 3752.

(76) Schwegmann, S.; Seitsonen, A. P.; De Renzi, V.; Dietrich, H.; Bludau, H.; Gierer, M.; Over, H.; Jacobi, K.; Scheffler, M.; Ertl, G. *Phys. Rev. B* **1998**, *57*, 15487.
(77) Batamack, P.; Vincent, R.; Fraissard, J. *Catal. Lett.* **1996**, *36*, 81.
(78) Alam, T. M.; Nyman, M.; Cherry, B. R.; Segall, J. M.; Lybarger, L. E. *J. Am. Chem. Soc.* **2004**, *126*, 5610.
(79) Reddy, B. M.; Reddy, E. P.; Srinivas, S. T.; Mastikhin, V. M.; Nosov, A. V.; Lapina, O. B. *J. Phys. Chem.* **1992**, *96*, 7076.
(80) Leboda, R.; Turov, V. V.; Marciniak, M.; Malygin, A. A.; Malkov, A. A. *Langmuir* **1999**, *15*, 3148.
(81) Kim, K. S.; Baitinger, W. E.; Amy, J. W.; Winograd, N. *J. Electron. Spectrosc. Relat. Phenom.* **1974**, *5*, 351.
(82) Chmiola, J.; Largeot, C.; Taberna, P. L.; Simon, P.; Gogotsi, Y. *Angew. Chem., Int. Ed.* **2008**, *47*, 3392.
(83) Chmiola, J.; Yushin, G.; Dash, R.; Gogotsi, Y. *J. Power Sources* **2006**, *158*, 765.
(84) Chmiola, J.; Yushin, G.; Gogotsi, Y.; Portet, C.; Simon, P.; Taberna, P. L. *Science* **2006**, *313*, 1760.
(85) Largeot, C.; Portet, C.; Chmiola, J.; Taberna, P. L.; Gogotsi, Y.; Simon, P. *J. Am. Chem. Soc.* **2008**, *130*, 2730.

AM9007903